Gravitational radiation from coalescing binary neutron stars

Xing Zhuge, Joan M. Centrella, and Stephen L. W. McMillan
Department of Physics and Atmospheric Science, Drexel University, Philadelphia, Pennsylvania 19104
(Received 22 April 1994)

We calculate the gravitational radiation produced by the merger and coalescence of inspiraling binary neutron stars using three-dimensional numerical simulations. The stars are modeled as polytropes and start out in the point-mass limit at wide separation. The hydrodynamic integration is performed using smooth particle hydrodynamics with Newtonian gravity, and the gravitational radiation is calculated using the quadrupole approximation. We have run several simulations, varying both the neutron-star radius and the equation of state. The resulting gravitational wave energy spectra dE/df are rich in information about the hydrodynamics of merger and coalescence. In particular, our results demonstrate that detailed information on both GM/Rc^2 and the equation of state can in principle be extracted from the spectrum.

PACS number(s): 04.30.Db, 04.80.Nn, 97.60.Jd, 97.80.−d

I. INTRODUCTION

Coalescing binary neutron stars are among the most promising sources of gravitational waves for detection by interferometers such as Laser Interferometric Gravitational Wave Observatory (LIGO) and VIRGO [1,2]. Recent studies [3] suggest that binary inspiral due to gravitational radiation reaction, and the eventual coalescence of the component stars, may be detectable by these instruments at a rate of several per year. The inspiral phase comprises the last several thousand binary orbits and covers the frequency range $f \sim 10$–1000 Hz, where the broadband interferometers are most sensitive. During this stage, the separation of the stars is much larger than their radii and the gravitational radiation can be calculated quite accurately using post-Newtonian expansions in the point-mass limit [4]. It is expected that the inspiral wave form will reveal the masses and spins of the neutron stars, as well as the orbital parameters of the binary systems [2,5,6].

When the binary separation is comparable to the neutron star radius, hydrodynamic effects become dominant and coalescence takes place within a few orbits. The coalescence regime probably lies at or beyond the upper end of the frequency range accessible to broadband detectors, but it may be observed using specially designed narrow band interferometers [7] or resonant detectors [8]. Such observations may yield valuable information about neutron star radii, and thereby the nuclear equation of state [5,9,10].

Three-dimensional numerical simulations are needed to calculate the detailed hydrodynamical evolution of the system during coalescence. Rather than dwell on the uncertain details of the physics of neutron-star interiors, most studies of this problem have opted simply to model the neutron stars as polytropes with the equation of state

$$P = K\rho^{\Gamma} = K\rho^{1+1/n}, \tag{1}$$

where K is a constant that measures the specific entropy of the material and n is the polytropic index. A choice of $n = 1$ ($\Gamma = 2$) mimics a fairly stiff nuclear equation of state. Shibata, Nakamura, and Oohara [11,12] have studied the behavior of binaries with both synchronously rotating and nonrotating stars, using an Eulerian code with gravitational radiation reaction included. Rasio and Shapiro [13,14] have simulated the coalescence of synchronously rotating neutron-star binaries using the Lagrangian smooth particle hydrodynamics (SPH) method with purely Newtonian gravity. Recently, Davies *et al.* [15] have carried out SPH simulations of the inspiral and coalescence of nonsynchronously rotating neutron stars, focusing on the thermodynamics and nuclear physics of the coalescence, with particular application to γ-ray bursts. All of these studies use the quadrupole formula to calculate the gravitational radiation emitted.

Stars in a synchronous binary rotate in the same sense as their orbital motion, with spin angular velocity equal to the orbital angular velocity, as seen from a nonrotating frame. In most close binary systems (for example, those with normal main-sequence components) viscosity acts to spin up initially nonrotating stars, causing them to come into a state of synchronous rotation in a relatively short period of time [16]. However, realistic neutron-star viscosities are expected to be quite small, and recent work suggests [17] that the time scale for synchronization of neutron-star binaries is generally much longer than the time scale for orbital decay and inspiral due to the emission of gravitational waves. Thus neutron-star binaries are generally *not* expected to become synchronous as they evolve toward coalescence.

As a complement to full three-dimensional (3D) hydrodynamical simulations, Lai, Rasio, and Shapiro [18,19] have used quasiequilibrium methods to focus on the last 10 or so orbits before the surfaces of the neutron stars come into contact. During this time, as tidal effects grow, the neutron stars are modeled as triaxial ellipsoids inspiraling on a sequence of quasistatic circular orbits. Using an approximate energy variational method these authors have modeled both synchronous and nonsynchronous binaries. They find that, for sufficiently incompressible

polytropes ($n < 1.2$), the system undergoes a dynamical instability which can significantly accelerate the secular orbital inspiral driven by radiation reaction. (This instability is driven by Newtonian hydrodynamics; see [20] for the case of an unstable plunge driven by strong spacetime curvature.) They have calculated the evolution of binaries as they approach the stability limit and the orbital decay changes from secular to dynamical in character, and have investigated the resulting gravitational wave emission [18]. Their results provide an important component in understanding the behavior of the full 3D hydrodynamical models.

We have carried out 3D simulations of the coalescence of nonrotating neutron stars using SPH, with particular application to the resulting gravitational wave-energy spectrum dE/df. Our initial conditions consist of identical spherical polytropes of mass M and radius R on circular orbits with separations sufficiently large that tidal effects are negligible. The stars thus start out effectively in the point-mass regime. The gravitational field is purely Newtonian, with gravitational radiation calculated using the quadrupole approximation. To cause the stars to spiral in, we mimic the effects of gravitational radiation reaction by introducing a frictional term into the equations of motion to remove orbital energy at the rate given by the equivalent point-mass inspiral. As the neutron stars get closer together the tidal distortions grow and eventually dominate, and coalescence quickly follows. The resulting gravitational wave forms match smoothly onto the point-mass inspiral wave forms, facilitating analysis in the frequency domain. We focus on examining the effects of changing R and the polytropic index n on the gravitational wave-energy spectrum dE/df.

This paper is organized as follows. In Section II we present a brief description of the numerical techniques we used to do the simulations. Section III discusses the calculation of the gravitational wave quantities, including the spectrum dE/df. The use of a frictional term in the equations of motion to model the inspiral by gravitational radiation reaction is discussed in Sec. IV, and the initial conditions are given in Sec. V. The results of binary inspiral and coalescence for a standard run with $M = 1.4\ M_\odot$, $R = 10$ km, and polytropic index $n = 1$ ($\Gamma = 2$) are given in Sec. VI, with the frequency analysis and the spectrum dE/df presented in Sec. VII. Section VIII presents the results of varying the neutron-star radius R and the polytropic index n. Finally, Sec. IX contains a summary of our results.

II. NUMERICAL TECHNIQUES

Lagrangian methods such as SPH [21] are especially attractive for modeling neutron-star coalescence since the computational resources can be concentrated where the mass is located instead of being spread over a grid that is mostly empty. We have used the implementation of SPH by Hernquist and Katz [22] known as TREESPH. In this code, the fluid is discretized into particles of finite extent described by a smoothing kernel. The use of variable smoothing lengths and individual particle time steps makes the program adaptive in both space and time.

Gravitational forces in TREESPH are calculated using a hierarchical tree method [23] optimized for vector computers. In this method, the particles are first organized into a nested hierarchy of cells, and the mass multipole moments of each cell up to a fixed order, usually quadrupole, are calculated. To compute the gravitational acceleration, each particle interacts with different levels of the hierarchy in different ways. The force due to neighboring particles is computed by directly summing the two-body interactions. The influence of more distant particles is taken into account by including the multipole expansions of the cells which satisfy the accuracy criterion at the location of each particle. In general, the number of terms in the multipole expansions is small compared to the number of particles in the corresponding cells. This leads to a significant gain in efficiency and allows the use of larger numbers of particles than would be possible with methods that simply sum over all possible pairs of particles.

TREESPH uses artificial viscosity to handle the shocks that develop when stars collide and coalesce. The code contains three choices for the artificial viscosity; we have chosen to use the version modified by the curl of the velocity field. This prescription reduces the amount of artificial viscosity used in the presence of curl, and has proved to be superior to the other options in tests of head-on collisions of neutron stars [24] and global rotational instability [25]. Since this has already been discussed in the literature, we remark only that the artificial viscosity consists of two terms, one that is linear in the particle velocities (with user-specified coefficient α) and another that is quadratic in the velocities (with coefficient β), and refer the interested reader to Refs. [22] and [24] [see especially their Eqs. (3), (5), and (6)] for details.

As has been noted above, the neutron stars are not expected to be synchronously rotating due to their very small physical viscosity. However, in computer simulations numerical viscosity, either present in the method itself or added explicitly as artificial viscosity, can have a similar effect and cause the stars to spin up. We have monitored this effect in our simulations and have found it to be small; see Sec. VI below.

III. CALCULATION OF GRAVITATIONAL RADIATION

The gravitational radiation in our simulations is calculated in the quadrupole approximation, which is valid for nearly Newtonian sources [26]. The gravitational waveforms are the transverse-traceless (TT) components of the metric perturbation h_{ij}:

$$h_{ij}^{\mathrm{TT}} = \frac{G}{c^4}\frac{2}{r}\ddot{I}_{ij}{}^{\mathrm{TT}}, \tag{2}$$

where

$$I_{ij} = \int \rho\,(x_i x_j - \tfrac{1}{3}\delta_{ij} r^2)\,d^3r \tag{3}$$

is the reduced (i.e., traceless) quadrupole moment of the source and an overdot indicates a time derivative d/dt. Here spatial indices $i,j = 1,2,3$ and the distance to the source $r = (x^2+y^2+z^2)^{1/2}$. In an orthonormal spherical coordinate system (r,θ,ϕ) with the center of mass of the source located at the origin, the TT part of I_{ij} has only four nonvanishing components. Expressed in terms of Cartesian components these are (cf. [27])

$$\begin{aligned} I_{\theta\theta} &= (I_{xx}\cos^2\phi + I_{yy}\sin^2\phi + I_{xy}\sin 2\phi)\cos^2\theta \\ &\quad + I_{zz}\sin^2\theta - (I_{xz}\cos\phi + I_{yz}\sin\phi)\sin 2\theta, \\ I_{\phi\phi} &= I_{xx}\sin^2\phi + I_{yy}\cos^2\phi - I_{xy}\sin 2\phi, \\ I_{\theta\phi} &= I_{\phi\theta} \\ &= \tfrac{1}{2}(I_{yy} - I_{xx})\cos\theta\sin 2\phi + I_{xy}\cos\theta\cos 2\phi \\ &\quad + (I_{xz}\sin\phi - I_{yz}\cos\phi)\sin\theta. \end{aligned} \tag{4}$$

The wave amplitudes for the two polarizations are then given by

$$h_+ = \frac{G}{c^4}\frac{1}{r}(\ddot{I}_{\theta\theta} - \ddot{I}_{\phi\phi}), \tag{5}$$

$$h_\times = \frac{G}{c^4}\frac{2}{r}\ddot{I}_{\theta\phi}. \tag{6}$$

For an observer located on the axis at $\theta = 0, \phi = 0$ these reduce to

$$h_{+,\mathrm{axis}} = \frac{G}{c^4}\frac{1}{r}(\ddot{I}_{xx} - \ddot{I}_{yy}), \tag{7}$$

$$h_{\times,\mathrm{axis}} = \frac{G}{c^4}\frac{2}{r}\ddot{I}_{xy}. \tag{8}$$

The angle-averaged wave forms are defined by [27]

$$\langle h_+^2\rangle = \frac{1}{4\pi}\int h_+^2\, d\Omega, \qquad \langle h_\times^2\rangle = \frac{1}{4\pi}\int h_\times^2\, d\Omega, \tag{9}$$

which give

$$\begin{aligned} \frac{c^8}{G^2}r^2\langle h_+^2\rangle &= \tfrac{4}{15}(I_{xx}^{(2)} - I_{zz}^{(2)})^2 + \tfrac{4}{15}(I_{yy}^{(2)} - I_{zz}^{(2)})^2 \\ &\quad + \tfrac{1}{10}(I_{xx}^{(2)} - I_{yy}^{(2)})^2 + \tfrac{14}{15}(I_{xy}^{(2)})^2 \\ &\quad + \tfrac{4}{15}(I_{xz}^{(2)})^2 + \tfrac{4}{15}(I_{yz}^{(2)})^2, \\ \frac{c^8}{G^2}r^2\langle h_\times^2\rangle &= \tfrac{1}{6}(I_{xx}^{(2)} - I_{yy}^{(2)})^2 + \tfrac{2}{3}(I_{xy}^{(2)})^2 + \tfrac{4}{3}(I_{xz}^{(2)})^2 \\ &\quad + \tfrac{4}{3}(I_{yz}^{(2)})^2. \end{aligned} \tag{10}$$

[Note that Eq. (10) corrects some typographical errors in Eq. (3.12) of [27].]

The standard definition of gravitational-wave luminosity is

$$L = \frac{dE}{dt} = \frac{1}{5}\frac{G}{c^5}\left\langle\left\langle I_{ij}^{(3)}I_{ij}^{(3)}\right\rangle\right\rangle, \tag{11}$$

where there is an implied sum on i and j, the superscript (3) indicates the third-time derivative, and the double angle brackets indicate an average over several wave periods. Since such averaging is not well defined during coalescence, we simply display the unaveraged quantity $(G/5c^5)I_{ij}^{(3)}I_{ij}^{(3)}$ in the plots below. The energy emitted as gravitational radiation is

$$\Delta E = \int L\, dt. \tag{12}$$

The angular momentum lost to gravitational radiation is

$$\frac{dJ_i}{dt} = \frac{2}{5}\frac{G}{c^5}\epsilon_{ijk}\left\langle\left\langle I_{jm}^{(2)}I_{km}^{(3)}\right\rangle\right\rangle, \tag{13}$$

where ϵ_{ijk} is the alternating tensor. The total angular momentum carried away by the waves is

$$\Delta J_i = \int (dJ_i/dt)dt. \tag{14}$$

Again, we plot the unaveraged quantity $(2G/5c^5)\epsilon_{ijk}I_{jm}^{(2)}I_{km}^{(3)}$ for dJ_i/dt.

The energy emitted in gravitational waves per unit frequency interval dE/df is given by Thorne [28] in the form

$$\frac{dE}{df} = \frac{c^3}{G}\frac{\pi}{2}(4\pi r^2)f^2\langle|\tilde{h}_+(f)|^2 + |\tilde{h}_\times(f)|^2\rangle, \tag{15}$$

where r is the distance to the source and the angular brackets denote an average over all source angles. We define the Fourier transform $\tilde{h}(f)$ of any function $h(t)$ by

$$\tilde{h}(f) \equiv \int_{-\infty}^{+\infty} h(t)e^{2\pi i f t}dt \tag{16}$$

and

$$h(t) \equiv \int_{-\infty}^{+\infty} \tilde{h}(f)e^{-2\pi i f t}df. \tag{17}$$

To calculate the angle-averaged quantity $\langle|\tilde{h}_+|^2 + |\tilde{h}_\times|^2\rangle$, we first take the Fourier transforms of Eqs. (5) and (6), to obtain

$$\frac{c^4}{G}r\tilde{h}_+ = \tilde{I}_{\theta\theta}^{(2)} - \tilde{I}_{\phi\phi}^{(2)}, \tag{18}$$

$$\frac{c^4}{G}r\tilde{h}_\times = 2\tilde{I}_{\theta\phi}^{(2)}. \tag{19}$$

The Fourier transforms $\tilde{h}_+$ and $\tilde{h}_\times$ have the same angular dependence, given by (4), as h_+ and $h_\times$, respectively. The angle averaging

$$\langle|\tilde{h}_+|^2\rangle = \frac{1}{4\pi}\int|\tilde{h}_+|^2\, d\Omega, \qquad \langle|\tilde{h}_\times|^2\rangle = \frac{1}{4\pi}\int|\tilde{h}_\times|^2\, d\Omega \tag{20}$$

gives expressions analogous to (10):

$$\frac{c^8}{G^2}r^2\langle|\tilde{h}_+|^2\rangle = \tfrac{4}{15}|\tilde{I}^{(2)}_{xx} - \tilde{I}^{(2)}_{zz}|^2 + \tfrac{4}{15}|\tilde{I}^{(2)}_{yy} - \tilde{I}^{(2)}_{zz}|^2 + \tfrac{1}{10}|\tilde{I}^{(2)}_{xx} - \tilde{I}^{(2)}_{yy}|^2 + \tfrac{14}{15}|\tilde{I}^{(2)}_{xy}|^2 + \tfrac{4}{15}|\tilde{I}^{(2)}_{xz}|^2 + \tfrac{4}{15}|\tilde{I}^{(2)}_{yz}|^2, \quad (21)$$

$$\frac{c^8}{G^2}r^2\langle|\tilde{h}_\times|^2\rangle = \tfrac{1}{6}|\tilde{I}^{(2)}_{xx} - \tilde{I}^{(2)}_{yy}|^2 + \tfrac{2}{3}|\tilde{I}^{(2)}_{xy}|^2 + \tfrac{4}{3}|\tilde{I}^{(2)}_{xz}|^2 + \tfrac{4}{3}|\tilde{I}^{(2)}_{yz}|^2.$$

We then have

$$\langle|\tilde{h}_+(f)|^2 + |\tilde{h}_\times(f)|^2\rangle = \langle|\tilde{h}_+(f)|^2\rangle + \langle|\tilde{h}_\times(f)|^2\rangle, \quad (22)$$

which may be substituted into expression (15) for dE/df.

We use the techniques of [24] to calculate the quadrupole moment and its derivatives. In particular, $\ddot{I}$ and $\dddot{I}$ are obtained using particle positions, velocities, and accelerations already present in the code to produce very smooth wave forms. This yields expressions similar to those of Finn and Evans [29]. However, $I^{(3)}_{ij}$ requires the derivative of the particle accelerations, which is taken numerically, and introduces some numerical noise into L and dJ_i/dt. This noise can be removed by smoothing; see [24] for further discussion. We have applied this smoothing in producing all graphs of L and dJ_i/dt in this paper.

IV. MODELING INSPIRAL BY GRAVITATIONAL RADIATION REACTION

Widely separated binary neutron stars (that is, with separation $a \gg R$) spiral together due to the effects of energy loss by gravitational radiation reaction. Once the two stars are close enough for tidal distortions to be significant, these effects dominate and rapid inspiral and coalescence ensue. In our calculations we initially place the neutron stars on (nearly) circular orbits with wide enough separation so that tidal distortions are negligible and the stars are effectively in the point-mass limit. Since the gravitational field is purely Newtonian and does not take radiation reaction losses into account, we must explicitly include these losses to cause inspiral until purely hydrodynamical effects take over.

To accomplish this, we add a frictional term to the particle acceleration equations to remove orbital energy at a rate given by the point-mass inspiral expression (see [15] for a similar approach). The gravitational wave luminosity for point-mass inspiral on circular orbits is [26,30]

$$L_{\rm PM} = \left.\frac{dE}{dt}\right|_{\rm PM} = \frac{32}{5}\frac{G^4}{c^5}\frac{\mu^2\mathcal{M}^3}{a^5}, \quad (23)$$

where $\mu = M_1M_2/(M_1+M_2)$ is the reduced mass, $\mathcal{M} = M_1+M_2$ is the total mass of the system, and the subscript "PM" refers to point-mass inspiral. For equal mass stars with $M_1 = M_2 \equiv M$ and separation $a = \xi R$, we find

$$\left.\frac{dE}{dt}\right|_{\rm PM} = \frac{64}{5}\frac{c^5}{G}\frac{1}{\xi^5}\left(\frac{GM}{c^2R}\right)^5. \quad (24)$$

We then assume that this energy change is due to a frictional force $\mathbf{f}$ that is applied at the center of mass of each star, so that each point in the star feels the same frictional deceleration. Dividing the loss equally between the two stars gives

$$\mathbf{f}\cdot\mathbf{V} = \frac{1}{2}\left.\frac{dE}{dt}\right|_{\rm PM}, \quad (25)$$

where $\mathbf{V}$ is the center of mass velocity of the star. Since $\mathbf{f}$ acts in the direction opposite to $\mathbf{V}$, this gives an acceleration

$$\mathbf{a} = \frac{\mathbf{f}}{M} = -\frac{1}{2M}\left.\frac{dE}{dt}\right|_{\rm PM}\frac{\mathbf{V}}{|\mathbf{V}|^2}. \quad (26)$$

This term is added to the acceleration of every particle, so that each particle in either star experiences the same frictional deceleration. The net effect is that the centers of mass of the stars follow trajectories that approximate point-mass inspiral. This frictional term is applied until tidal effects dominate, leading to more rapid inspiral and coalescence; see Sec. VI and Fig. 10 below. (Operationally, our assignment of a particle to a "star" is based simply on which body it happened to belong to initially. Since the frictional term is turned off before coalescence occurs, the question of what to do after the stars have merged does not arise.)

The dynamics of polytropes in purely Newtonian gravity is scale free in the sense that, for a given polytropic index n, the results of a calculation can be scaled for any values of the mass M and radius R. Inspiral by gravitational radiation reaction introduces the dimensionless parameter GM/Rc^2, as is explicitly evident in Eqs. (24) and (31) for our frictional model of inspiral. For neutron stars, GM/Rc^2 is determined by the nuclear equation of state. In the calculations below, we will vary both R (and hence GM/Rc^2) and the polytropic index n.

V. INITIAL CONDITIONS

Since our neutron stars start out widely separated with negligible tidal interaction, they are modeled initially as spherical polytropes. Because the time scale for tidal effects to develop is much greater than the dynamical time t_D for an individual star, where

$$t_D = \left(\frac{R^3}{GM}\right)^{1/2}, \quad (27)$$

we start with stable, "cold" polytropes produced by the method discussed in [24]. The stars are then placed on a circular orbit with separation $a_0 = \xi_0 R$ in the center-of-mass frame of the system in the x-y plane. Locating the centers of mass of the individual stars at (x,y) positions $(\pm a_0/2, 0)$ initially, the stars are then given the equivalent point-mass velocities for a circular orbit $V_y = \pm(M/2a_0)^{1/2}$.

To ensure that the stars start out on the correct point-mass inspiral trajectories, we also give them an initial inward radial velocity V_x as follows. For point-mass in-

spiral the separation $a(t)$ is given by [26]

$$a(t) = a_0 \left(1 - \frac{t}{\tau_0}\right)^{1/4}, \tag{28}$$

where a_0 is the separation at the initial time $t = 0$ and

$$\tau_0 = \frac{5}{256} \frac{c^5}{G^3} \frac{a_0^4}{\mu \mathcal{M}^2} \tag{29}$$

is the inspiral time, i.e., the time needed to reach separation $a = 0$. For equal mass stars, the initial inward velocity is thus

$$V_x = \left.\frac{dr}{dt}\right|_{t=0} = \frac{1}{2} \left.\frac{da}{dt}\right|_{t=0} = -\frac{1}{8} \frac{a_0}{\tau_0}. \tag{30}$$

Since the stars have initial separation $a_0 = \xi_0 R$, this gives

$$V_x = -\frac{64}{5} \frac{c}{\xi_0^3} \left(\frac{GM}{c^2 R}\right)^3. \tag{31}$$

The use of the correct initial inspiral trajectory allows us to match our gravitational wave forms smoothly to the equivalent point-mass wave forms. This is important when analyzing the signals in the frequency domain, as discussed in Sec. VII below.

VI. BINARY INSPIRAL AND COALESCENCE

We take the case $M = 1.4\ M_\odot$ and $R = 10$ km (so $GM/Rc^2 = 0.21$), with polytropic index $n = 1$ and initial separation $a_0 = 4R$ as our standard model, which we refer to as run 1. The parameters of this model and the other two models introduced in Sec. VIII below are presented in Table I. The results of the simulations are summarized in Table II. Time is measured in units of the dynamical time t_D given in Eq. (27); for run 1, $t_D = 7.3 \times 10^{-5}$ s.

The evolution of this system for the case of $N = 4096$ particles per star is shown in Fig. 1. Each frame shows the projection of all particles onto the x-y plane. As the stars spiral together, their tidal bulges grow. By $t \sim 100 t_D$ the stars have come into contact, after which they rapidly merge and coalesce into a rotating barlike structure. Note that the merger is a fairly gentle process and, in contrast to head-on collisions, does not generate strong shocks [14,24,31]. Spiral arms form as mass is shed from the ends of the bar. Gravitational torques cause angular momentum to be transported outward and lost to the spiral arms. The arms expand and eventually form a disk around the central object. By $t = 200 t_D$, the system is roughly axisymmetric.

Contour plots at $t = 200 t_D$ reveal more details of the system. In Fig. 2(a), which shows a cut along the x-y equatorial plane, we see that the core is essentially

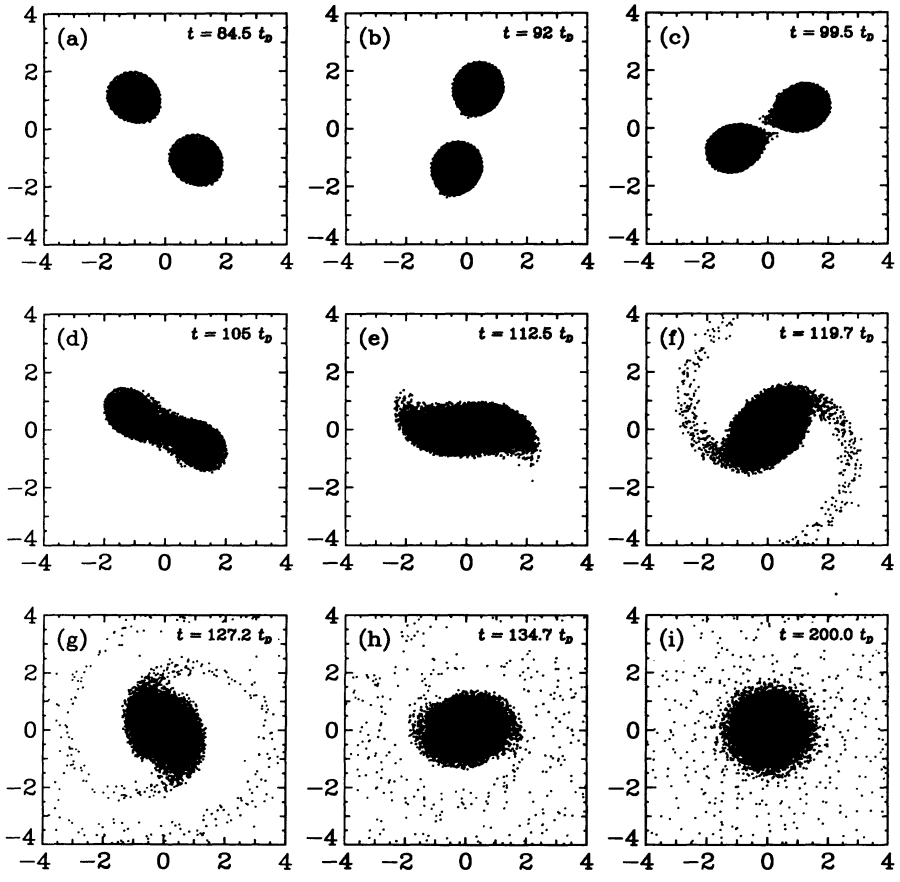

FIG. 1. Particle positions are shown projected onto the x-y plane for run 1 with $N = 4096$ particles per star. Here, $M = 1.4\ M_\odot$, $R = 10$ km, polytropic index $n = 1$, and initial separation $a_0 = 4R$. The stars are orbiting in the counterclockwise direction. The vertical axis in each frame is y/R and the horizontal axis is x/R.

axisymmetric out to cylindrical radius $\varpi \sim 2R$, where $\varpi = (x^2 + y^2)^{1/2}$. As the spiral arms wind up, expand, and merge, the disk grows increasingly axisymmetric. In the process the arms expand supersonically, producing shock heating that causes the disk to puff up. This can be seen in Fig. 2(b), which shows density contours (two per decade in density) for a cut along the meridional x-z plane.

The angular velocity $\Omega(\varpi)$ of the particles is shown as a function of cylindrical radius ϖ in Fig. 3. For our choice of parameters, $\Omega = 1$ (t_D^{-1}) corresponds to a spin period $T_{\rm spin} = 0.46$ ms. At $t = 150t_D$ the object is in the final stage of its gravitational wave "ring down" (cf. Fig. 6 below). Fig. 3(a) shows that the central core $\varpi \lesssim 2R$ is still differentially rotating at this time (with $\Omega \sim \varpi^{-0.4}$). The disk $\varpi \gtrsim 2R$ is also differentially rotating, with $\Omega \sim \varpi^{-2}$. By $t = 200t_D$ the central object has less differential rotation and is more nearly rigidly rotating, with $\Omega \sim 0.65t_D^{-1}$, giving a spin period $T_{\rm spin} \sim 0.71$ ms. The disk is differentially rotating with $\Omega \sim \varpi^{-1.7}$. (Recall that Keplerian motion has $\Omega \sim \varpi^{-1.5}$.)

The mass m contained within cylindrical radius ϖ is plotted in Fig. 4, showing that $\sim 6\%$ of the mass has been shed to the disk $\varpi \gtrsim 2R$. Between the times $t = 150t_D$ and $t = 200t_D$, some of the matter in the disk is redistributed out to larger radii. The specific spin angular momentum $j(\varpi)$ within cylindrical radius ϖ is shown in Fig. 5. About 27% of the angular momentum has been shed to the disk, with continued outward transport of angular momentum within the disk taking place between $t = 150t_D$ and $t = 200t_D$.

The gravitational wave forms rh_+ and $rh_\times$ for an observer on the axis at $\theta = 0$ and $\varphi = 0$ are shown for this run in Figs. 6(a) and 6(b), where the solid lines give the code wave forms and the dashed lines the point-mass results. For the first couple of orbits after the start of the run ($T_{\rm orbit} = 2T_{\rm GW}$) the code wave forms match the point-mass predictions. As the tidal bulges grow, the stars spiral in faster than they would on point-mass trajectories, leading to an increase in the frequency and amplitude of the gravitational wave forms (cf. [18]). The gravitational wave amplitudes reach a maximum during

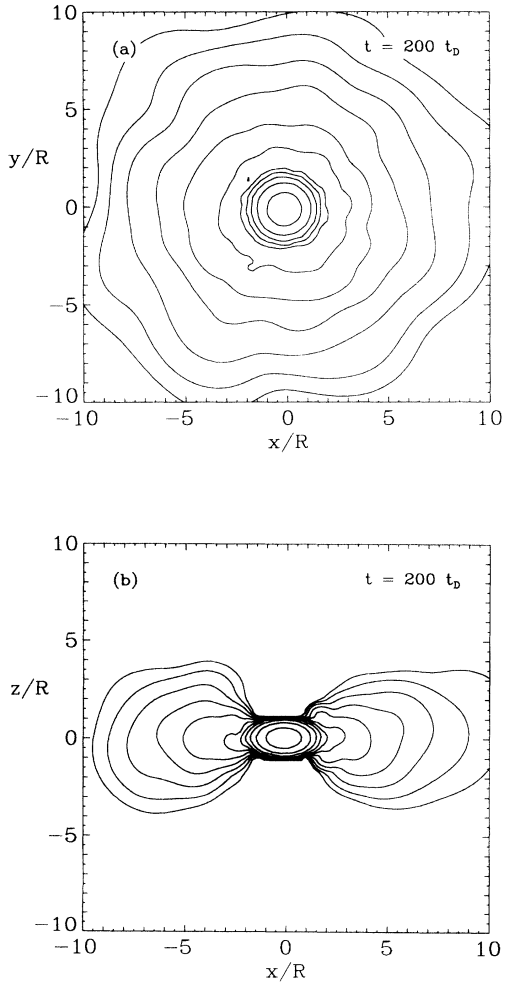

FIG. 2. (a) Density contours are shown for a cut along the x-y plane for run 1 with $N = 4096$ particles per star at $t = 200t_D$. The contour levels are 0.3, 0.1, 0.03, 0.01, ... (the central density is $0.6M/R^3$). (b) The same density contours as in part (a), but for a cut along the x-z plane.

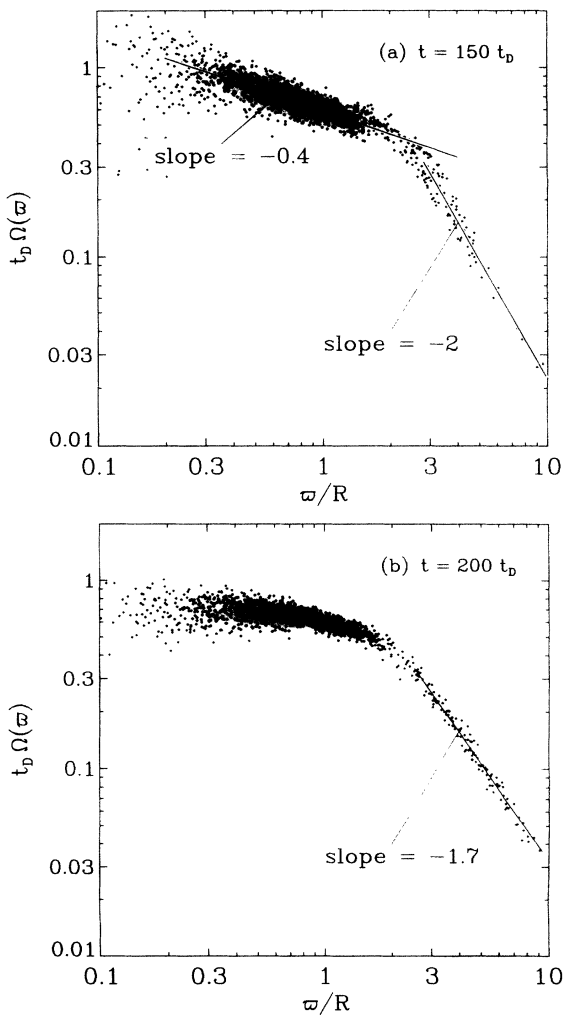

FIG. 3. The angular velocity $\Omega(\varpi)$, where $\varpi = (x^2 + y^2)^{1/2}$, is shown for run 1 with $N = 4096$ particles per star. $\Omega = 1$ (i.e., t_D^{-1}) corresponds to a spin period $T_{\rm spin} = 0.46$ ms. (a) $t = 150t_D$, (b) $t = 200t_D$.

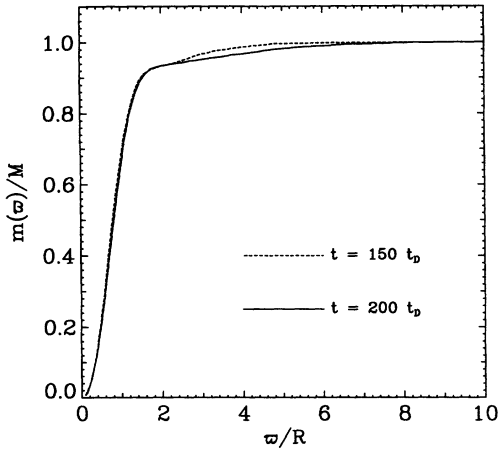

FIG. 4. The mass fraction $m(\varpi)$ is shown at $t = 150t_D$ and $t = 200t_D$ for run 1 with $N = 4096$ particles per star.

the merger of the two stars at $t \sim 105 - 110t_D$, then decrease as the stars coalesce and the spiral arms expand and form the disk. The peak wave-form amplitude $(c^2/GM)rh_+ \sim 0.4$ corresponds to a value $h \sim 1.4 \times 10^{-21}$ for a source at distance $r = 20$ Mpc (the approximate distance to the Virgo cluster). By $t \sim 180t_D$ the gravitational waves have shut off and the system is essentially axisymmetric.

Figure 7(a) shows the gravitational wave luminosity L/L_0 (where $L_0 = c^5/G$) , 7(b) the energy $\Delta E/Mc^2$ emitted as gravitational radiation, 7(c) dJ_z/dt for the gravitational radiation, and 7(d) the total angular momentum $\Delta J_z/J$ (where J is the initial total angular momentum of the system) carried by the waves. In all the gravitational-wave quantities, the code results (solid lines) initially track the point-mass case (dashed lines) very well, departing significantly from the point-mass predictions somewhat before the onset of dynamical instability. The maximum luminosity is $1.65 \times 10^{-4}L_0$. This may be compared with the value of $5.3 \times 10^{-4}L_0$ found by [24] for the case of a head-on collision with $GM/Rc^2 = 0.21$; for off-axis collisions on parabolic orbits, the maximum obtained by those authors was $1.0 \times 10^{-3}L_0$. The total energy radiated away after the luminosity departs from the point-mass result by more than 10% is $0.032Mc^2$. Again this can be compared with $0.0025Mc^2$ for a head-on collision and a maximum of $0.016Mc^2$ for off-axis collisions obtained by [24]. Although the collisions can achieve a higher gravitational-wave luminosity, they radiate less energy in the form of gravitational waves overall because they take place on shorter time scales than the inspiralling binaries.

How sensitive are these results to the resolution of the calculation? To answer this question we ran the same standard model with different numbers of particles per star. Figure 8 shows a comparison of the wave form rh_+ for the cases $N = 1024$, 2048, and 4096 particles per star. It is clear that the differences in the wave forms are small. We will see in Sec. VII below that there are only slight differences in the frequency domain as well.

In numerical simulations viscosity, whether implicit in the numerical method or added explicitly as artificial vis-

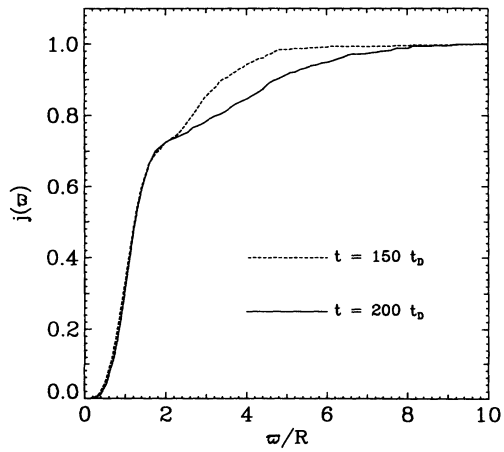

FIG. 5. The specific angular momentum $j(\varpi)$, normalized to unity for the entire system, is shown at $t = 150t_D$ and $t = 200t_D$ for run 1 with $N = 4096$ particles per star.

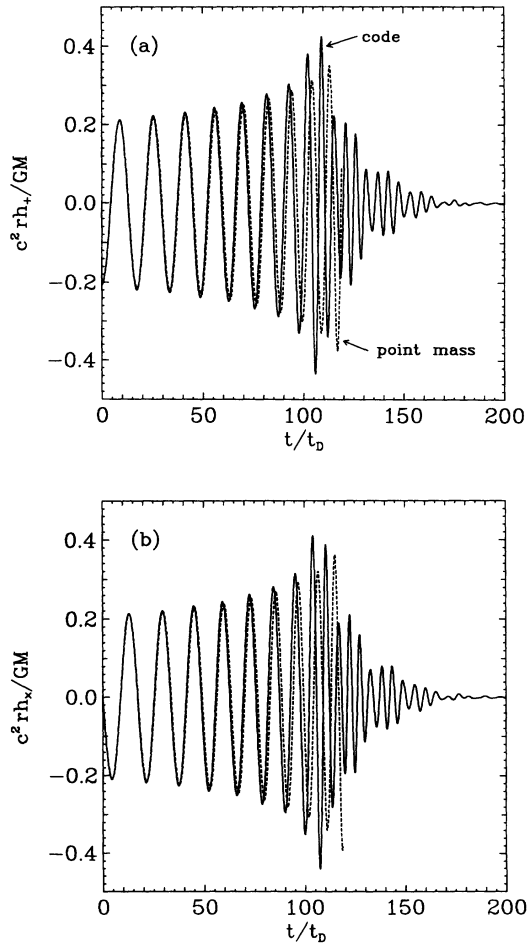

FIG. 6. The gravitational wave forms rh_+ and $rh_\times$ are shown for an observer on the axis at $\theta = 0$, $\phi = 0$ for run 1 with $N = 4096$ particles per star. The solid lines give the code wave forms, and the dashed lines the point-mass results.

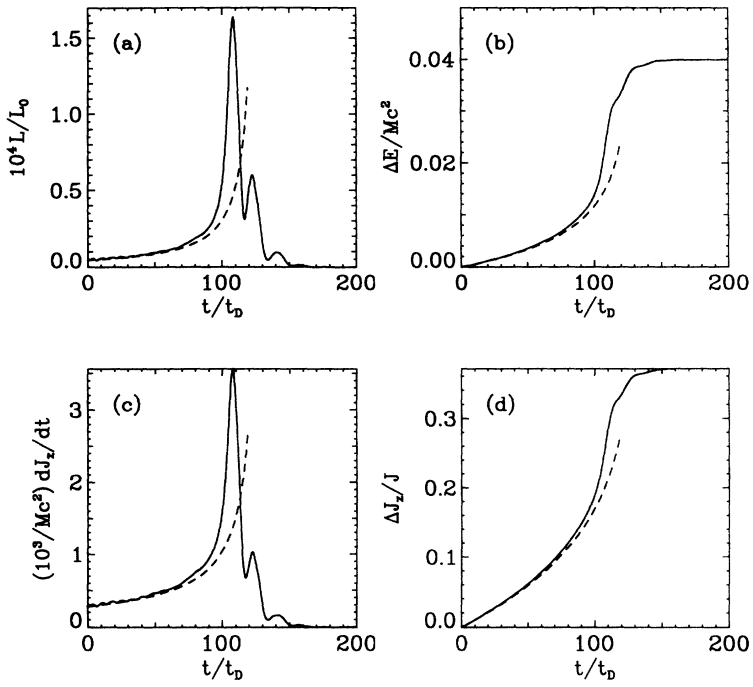

FIG. 7. Various gravitational radiation quantities are shown for run 1 with $N = 4096$ particles per star. The solid lines show the code results, and the dashed lines the point-mass values. (a) Gravitational wave luminosity L/L_0, where $L_0 = c^5/G$; (b) energy $\Delta E/Mc^2$ emitted as gravitational radiation; (c) dJ_z/dt; (d) the angular momentum $\Delta J_z/J$ carried away by the waves, where J is the initial total angular momentum of the system.

cosity, can cause problems by artificially spinning up the stars [15]. To monitor this effect in our simulations we calculated the spin angular momentum of each star about its center of mass and compared this with the results expected for a synchronously rotating star (the expected result in the limit of large viscosity). In general, we have found that these nonphysical viscous effects always remain small in our simulations. For example, we ran a test case consisting of initially nonspinning stars each composed of $N = 1024$ particles on a circular orbit of constant separation $a = 4R$, with artificial viscosity coefficients $\alpha = \beta = 0.3$. After $100t_D$ (~ 2.8 orbits), the stars had spin angular momenta $< 2.3\%$ of the synchronous value. We conclude that numerical and artificial viscosities play negligible roles in spinning up the stars in our simulations.

For inspiraling stars, torquing due to the gravitationally induced tidal bulges will cause a physical spin up of the stars [14]. This is shown for the case $N = 4096$ particles per star in Fig. 9, which plots the spin angular momentum of one star (normalized by the spin of a synchronously rotating star at that orbital separation) as a function of time. We see that the spin angular mo-

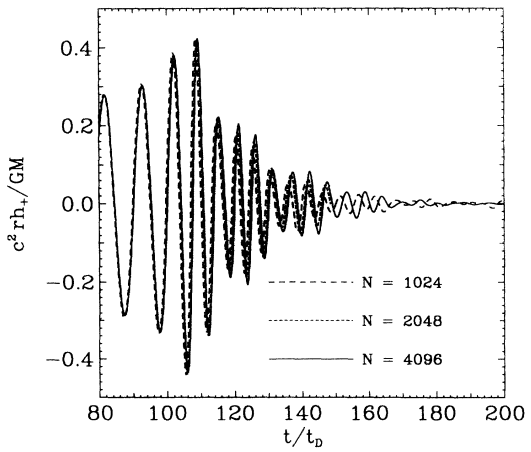

FIG. 8. A comparison of the wave form rh_+ for run 1 using $N = 1024$, 2048, and 4096 particles per star. The case $N = 2048$ particles per star was only run for $150t_D$.

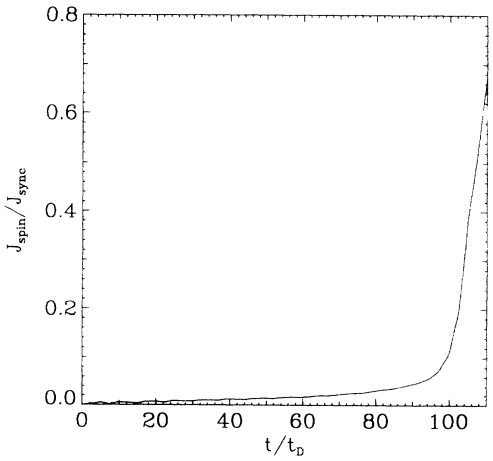

FIG. 9. The ratio of J_{spin}, the spin angular momentum of a star, to J_{sync}, the value for a synchronously rotating star at that separation, is plotted vs time for run 1 with $N = 4096$ particles per star. This graph shows that artificial viscosity does not significantly spin up the star during the inspiral. By $t \sim 100t_D$ the stars are in contact, and the rapid spin up is due to gravitationally induced tidal torquing during the merger process.

mentum of the star remains small until contact occurs at $t \sim 100t_D$; after this it increases sharply, reaching nearly 70% of the synchronous value at $t = 105t_D$. (Each "star" is composed of the particles that belonged to it initially, with the orbital separation of the stars given by the distance between the two centers of mass.) Comparison with Fig. 1 confirms that this effect is due to the tidal torquing that occurs when the stars develop large tidal bulges, come into contact, and merge.

Once the stars are close enough for this gravitationally induced tidal torquing to be significant, Newtonian gravitational effects operating on a dynamical time scale dominate the secular radiation reaction effects, leading to more rapid inspiral, merger, and coalescence [18]. We should turn off the gravitational friction term at some time after the Newtonian tidal torquing takes over and before the merger occurs, since during the merger the concept of equivalent point-mass trajectories is meaningless. We have experimented with turning off the gravitational friction term at different times and present the results for our standard run with $N = 1024$ particles per star in Fig. 10, which shows the center-of-mass separation of the two stars as a function of time. Here, the solid line shows the result of running with the gravitational friction term left on, and the short dashed lines show the results of turning this term off at (1) $t = 70t_D$, (2) $t = 85t_D$, and (3) $t = 100t_D$. The long-dashed line shows the equivalent point-mass result.

In cases (1) and (2), the stars go into nearly circular orbits (with eccentricities appropriate to the inspiral radial velocity at that separation) once the frictional term is turned off. However, the trajectory in case (3) is very similar to the result when the frictional term is left on, indicating that the Newtonian tidal effects are dominant by this point. The center-of-mass separation of the two stars in this case is $\sim 2.5R$ at $t = 100t_D$, and then rapidly decreases. This result is in good agreement with the prediction of a dynamical stability limit

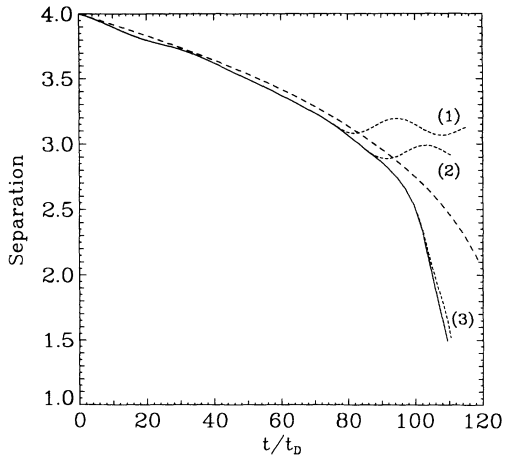

FIG. 10. The separation between the centers of mass of the stars for run 1 with $N = 1024$ particles per star is shown. The solid line gives the result of leaving the gravitational friction term on. The short-dashed lines show the effect of turning off the friction term at (1) $t = 70t_D$, (2) $t = 85t_D$, and (3) $t = 100t_D$. The long-dashed line shows the point-mass result.

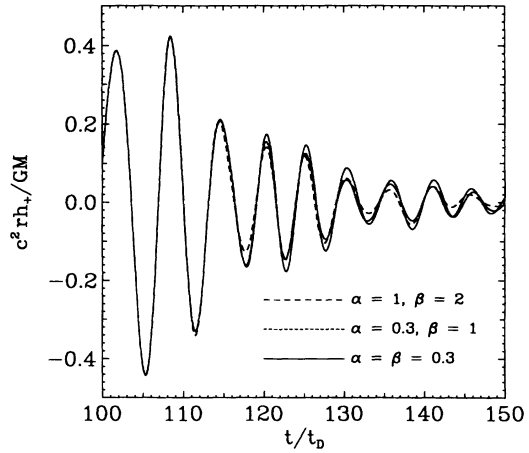

FIG. 11. The wave form rh_+ is shown for run 1 with $N = 1024$ particles per star with three different values of the artifical viscosity coefficients α and β.

at $a = 2.49R$ by Lai, Rasio, and Shapiro [18]. On the basis of these tests, we have turned off the gravitational friction term at $t = 100t_D$ for our standard run, and all the other plots in this paper for this run were done with this choice. For each of the runs reported below with different values of the physical parameters, we have carried out such experiments to determine the optimal time to turn off the gravitational friction term, since the time at which the Newtonian tidal effects dominate differs in each case (cf. [18]).

Finally, we have experimented with the values of the artificial viscosity coefficients α and β. For all runs we used the values $\alpha = \beta = 0.3$ during the inspiral phase. However, since shocks occur during the merger, coalescence, and the expansion of the spiral arms, we ran some tests with different amounts of artificial viscosity during these regimes. Figure 11 shows the wave form rh_+ for our standard run with $N = 1024$ particles per star during this phase for three cases: solid line, $\alpha = \beta = 0.3$; short-dashed line, $\alpha = 0.3$, $\beta = 1$; and long-dashed line, $\alpha = 1$, $\beta = 2$. Not surprisingly, the amplitude of the wave form is damped as α and β are increased. The low viscosity case conserves energy to $\sim 2\%$ during the period 100–$200t_D$ (after the frictional term is turned off), indicating that the evolution of the system is not dominated by strong shocks. Overall, the differences in energy conservation for the three cases are not significant. Therefore, since the low viscosity case produces the least damping of the wave form, we chose to use the values $\alpha = \beta = 0.3$ in all of our runs.

VII. ANALYSIS IN THE FREQUENCY DOMAIN

Broadband detectors such as LIGO and VIRGO should be able to measure the gravitational wave forms of inspiraling neutron star binaries in the frequency range $f \sim 10 - 1000$ Hz. Comparison of these signals with wave form templates derived from post-Newtonian analysis is expected to yield the neutron-star mass M [5,6]. It is

important to develop techniques to measure the neutron-star radius R since this information, coupled with M, can constrain the equation of state for nuclear matter [10].

The actual merger and coalescence stages are driven primarily by hydrodynamics and are expected to depend on both R and the equation of state, here parametrized by the polytropic index n. For most neutron-star binaries, this will take place at frequencies $f > 1000$ Hz. In this regime, shot noise limits the sensitivity of the broadband interferometers and so these signals may not be detectable by them [1,2]. However, a set of specially designed narrow-band interferometers [7] or resonant detectors [8] may be able to provide information about this high frequency region [9].

The merger and coalescence of the neutron stars take place within several orbits following initial contact, after which the gravitational radiation shuts off fairly rapidly as the system settles into a roughly axisymmetric final state [5]. This rapid shutoff of gravitational waves is expected to produce a sharp cutoff in the spectrum dE/df. Since the frequency of the radiation calculated in the point-mass approximation at separation a scales as $\sim a^{-3/2} \sim R^{-3/2}$, a set of narrow-band detectors that can locate the cutoff frequency where the energy spectrum dE/df drops sharply may in principle determine the neutron-star radius R [5,9,32].

We have calculated the spectrum dE/df for our simulations using Eq. (15). For point-mass inspiral, $dE/df \sim f^{-1/3}$ [28], where the decrease in energy with frequency reflects the fact that the binary spends fewer cycles near a given frequency f as it spirals in. To see any cutoff frequency in our data, we need a reasonably long region of point-mass inspiral in the frequency domain. Although our runs do start out in the point-mass regime, the binaries undergo dynamical instability and rapid merger within just a few orbits. To compensate for this we match our wave forms h_+ and $h_\times$ onto point-mass wave forms extending back to much larger separations and hence lower frequencies.

The energy spectrum dE/df for run 1 with $N = 4096$ particles per star is shown in Fig. 12. The solid line shows the spectrum for the extended wave form including point-mass inspiral, and the short-dashed line shows the spectrum of the simulation data only. Note that the two curves match closely. The separation at which the data were matched corresponds to frequency ~ 770 Hz, which is well within the inspiral regime $dE/df \sim f^{-1/3}$. Figure 12 shows that the match is smooth, and does not affect the merger and coalescence region of the spectrum. We have also examined the effect of using different numbers of particles on dE/df. The result is shown in Fig. 13, which plots the spectra for run 1 with $N = 1024$ and 4096 particles per star. The use of a smaller number of particles makes only a slight difference to dE/df.

Examination of Figs. 12 and 13 reveals several interesting features. Starting in the point-mass regime, as f increases, dE/df first drops below the point-mass inspiral value, reaching a local minimum at $f \sim 1500$ Hz. We identify this initial dip with the onset of dynamical instability. For the parameters of run 1, Lai, Rasio, and Shapiro [18] found that dynamical instability occurs at

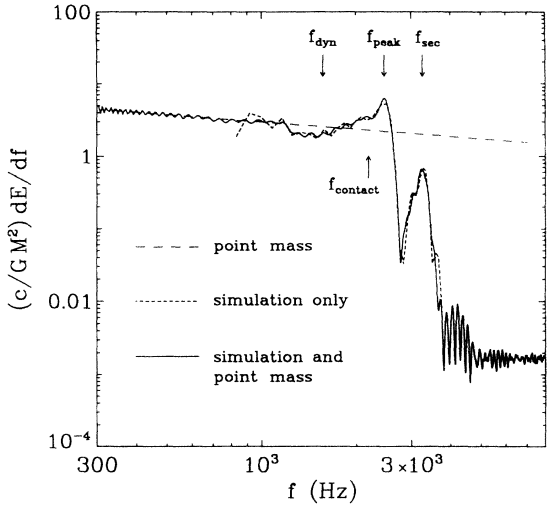

FIG. 12. The gravitational wave-energy spectrum dE/df is shown for run 1 with $N = 4096$ particles per star. The solid line shows the result of matching to point-mass inspiral, and the short-dashed line is the result of using the simulation data only. The long-dashed line shows dE/df for point-mass inspiral. The frequency $f_{dyn} = 1566$ Hz is the orbital frequency ($f_{GW} = 2f_{orb}$) at which dynamical instability occurs [18]. In addition, $f_{peak} \sim 2500$ Hz and $f_{sec} \sim 3200$ Hz mark the frequencies of the initial and secondary peaks, respectively. The frequency $f_{contact}$ corresponding to a circular point-mass orbit at separation $2R$ is also noted.

separation $a = 2.49R$; for point-mass inspiral, the frequency at this separation is $f_{dyn} = 1566$ Hz. The instability causes the spectrum dE/df to drop below the point-mass value, since the stars fall together faster than they would had they remained on strictly point-mass trajectories. For reference, Fig. 12 also shows the frequency $f_{contact} = (1/2\pi)(GM/R^3)^{1/2} \sim 2200$ Hz, which is twice

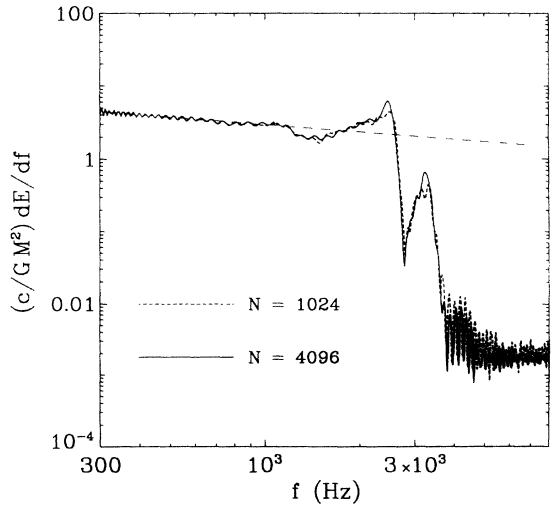

FIG. 13. The gravitational wave energy spectrum dE/df is shown for run 1 with $N = 4096$ particles per star (solid line) and $N = 1024$ particles per star (dashed line).

the orbital frequency (in the point-mass limit) at separation $2R$.

This initial falloff in the spectrum is rather slight. At higher frequencies, dE/df increases above the point-mass result, reaching a fairly broad maximum at $f_{\rm peak} \sim 2500$ Hz, roughly the frequency of the waves in Fig. 6 near $t \sim 125t_D$ (the approximate time at which the gravitational waves shut off). To further demonstrate that this feature is associated with the late-time behavior of the merged system, we have calculated the spectrum dE/df for the cases in which the wave forms rh_+ and $rh_\times$ (including the point-mass inspiral) were truncated at $t = 120t_D$ and $t = 150t_D$. The results are shown in Fig. 14, where the solid line shows the spectrum for the complete wave forms and the dashed lines show the spectra for the truncated ones. We see that this peak forms between $t = 120t_D$ and $t = 150t_D$, and therefore associate it with the transient, rotating barlike structure formed immediately following coalescence; cf. Fig. 1. The angular speed of this structure is $\sim 0.65t_D^{-1}$ (see Fig. 3), which corresponds to gravitational radiation with frequencies near ~ 2800 Hz. The conclusion that $f_{\rm peak}$ is associated with a bar is strengthened by run 3 below, in which the bar survives for a much longer time and the peak is correspondingly stronger.

Beyond $f_{\rm peak}$, the spectrum drops sharply, eventually rising again to a secondary maximum at $f_{\rm sec} \sim 3200$ Hz, too high to be associated with the bar. Figure 14 shows that this peak also appears between $t = 120t_D$ and $t = 150t_D$. We attribute this broad, high-frequency feature to transient oscillations induced in the coalescing stars during the merger process—the result of low-order p modes with frequencies somewhat higher than the Kepler frequency in the merging object (see, e.g., [33]).

The three frequencies $f_{\rm dyn}$, $f_{\rm peak}$, and $f_{\rm sec}$ serve as a useful means of characterizing our runs. They are indicated on Fig. 12 and are presented in more detail in Table III below.

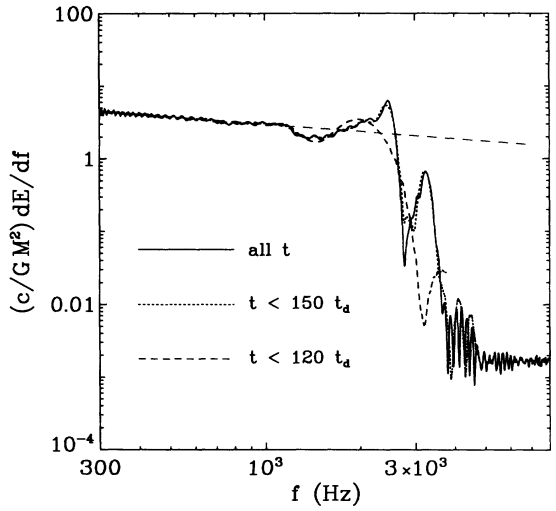

FIG. 14. The gravitational wave-energy spectrum dE/df is shown for run 1 with $N = 4096$ particles per star for the cases in which the wave forms were truncated at $t = 120t_D$ and $t = 150t_D$. The solid lines show the spectrum for the complete wave forms, while the dotted lines show the truncated cases.

VIII. THE EFFECTS OF CHANGING THE NEUTRON-STAR RADIUS AND EQUATION OF STATE

The energy spectrum dE/df shows rich structure in the frequency range $f \sim 1000 - 3000$ Hz in which the merger and coalescence of the neutron stars take place. To understand how observations of dE/df might provide information on the neutron-star radius and equation of state, we must investigate the effects of changing R and the polytropic index n. In this section we present the results of two runs which begin to explore this parameter space. We will continue this study in future papers.

Run 2 is the same as run 1 except that the initial neutron star radius is $R = 15$ km. Taking $M = 1.4\ M_\odot$, this gives $GM/Rc^2 = 0.14$; see Table I. This model was run with $N = 1024$ particles per star. The gross features of the evolution of this model are similar to those found in run 1. The stars first come into contact at $t \sim 250t_D$. By the end of the run, the core $\varpi \lesssim 2R$ is essentially axisymmetric and has 92% of the mass and 65% of the angular momentum. The disk extends out to $\sim 10R$. The gravitational wave forms rh_+ and $rh_\times$ are shown in Figs. 15(a) and 15(b) for an observer on the axis at $\theta = 0, \phi = 0$. Figure 16(a) shows the gravitational wave luminosity L/L_0 and 16(b) the energy $\Delta E/Mc^2$ emitted as gravitational radiation. As in Fig. 7, the time dependence of the angular momentum carried away by the waves is quite similar to that of the energy, and is not presented here. In these figures, the solid lines give the code wave forms and the dashed lines the point-mass results. Some interesting properties of this model are summarized in Table II.

The energy spectrum dE/df for run 2 is shown in Fig. 17. Again, we matched the code data to point-mass inspiral wave forms for analysis in the frequency domain. For run 2, the match occurs at frequency ~ 420 Hz. Given the parameters of this run, dynamical instability is expected to occur at separation $a = 2.49R$ [18]; the point-mass inspiral frequency at this separation is $f_{\rm dyn} = 852$ Hz. Figure 17 shows that, as in run 1, the spectrum drops below the point-mass inspiral result near $f_{\rm dyn}$. The spectrum does not then rise above the point-

TABLE I. Parameters of the models are given. Both the initial radius R and polytropic index n have been varied. The neutron-star mass is assumed to be $M = 1.4\ M_\odot$ in all cases. Run 1 was also run with $N = 1024$ and $N = 2048$ particles, as discussed in the text.

Model	R (km)	a_0	GM/Rc^2	t_D (ms)	n	Γ	N
Run 1	10	$4R$	0.21	0.073	1	2	4096
Run 2	15	$4R$	0.14	0.13	1	2	1024
Run 3	10	$4.5R$	0.21	0.073	0.5	3	1024

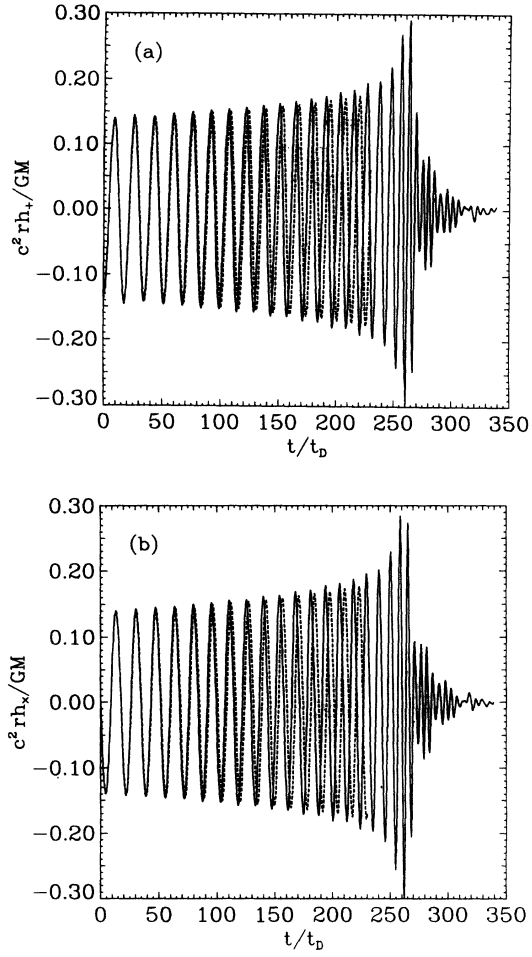

FIG. 15. The gravitational wave forms rh_+ and $rh_\times$ are shown for an observer on the axis at $\theta = 0$, $\phi = 0$ for run 2; compare with Fig. 6. The solid lines give the code wave forms, and the dashed lines the point-mass results.

mass result at $f_{\rm peak} \sim 1500$ Hz as in run 1; however, it does drop sharply just beyond $f_{\rm peak}$, rising again to a secondary peak at $f_{\rm sec} \sim 1750$ Hz. See Table III.

We estimate the frequency of the waves in Fig. 15 at the time when the gravitational radiation shuts off (around $t \sim 270t_D$) to be ~ 1300 Hz—that is, close to

TABLE II. Results of the simulations are summarized. The core mass $M_{\rm core}$ and angular momentum $J_{\rm core}$ refer to material with cylindrical radius $\varpi \lesssim 2R$. Peak values of the wave form $(c^2/GM)rh$ and luminosity L/L_0 are given; $(c^2/GM)rh \sim 0.4$ corresponds to a value $h \sim 1.4 \times 10^{-21}$ at distance $r = 20$ Mpc. The quantity $\Delta E/Mc^2$ is the energy lost to gravitational radiation after the stars depart significantly from the point-mass trajectory. It is still increasing at the end of run 3 due to the rotating nonaxisymmetric core.

Model	$M_{\rm core}$	$J_{\rm core}$	$(c^2/GM)rh$	L/L_0	$\Delta E/Mc^2$
Run 1	94%	73%	0.4	1.65×10^{-4}	0.032
Run 2	92%	65%	0.3	2.12×10^{-5}	0.013
Run 3	93%	67%	0.4	1.20×10^{-4}	> 0.042

$f_{\rm peak}$. The orbital angular velocity near the end of the run is $\Omega \sim 0.6t_D^{-1}$ or 4.5×10^3 rad/s; any residual nonaxisymmetric material rotating at this speed would yield gravitational waves at frequency $\sim$ 1500 Hz. Again, we interpret the secondary peak as the result of high-frequency oscillations in the merging system. The absence of a strong peak at $f_{\rm peak}$ and the weaker maximum at $f_{\rm sec}$ is the result of weaker tidal forces at the point of dynamical instability, leading to a less pronounced and shorter-lived bar.

Since the frequency of the gravitational radiation for point-mass inspiral is $\sim a^{-3/2} \sim R^{-3/2}$, we expect the features in the spectrum for run 2 to occur at lower frequencies than in run 1, roughly in the ratio $f_{\rm run\ 1}/f_{\rm run\ 2} \sim (R_{\rm run\ 1}/R_{\rm run\ 2})^{-3/2} \sim 1.8$. Our numerical simulations do indeed show this behavior. For example, the ratio of the frequencies at which the first peak occurs is $\sim$ 2500 Hz/1500 Hz $\sim$ 1.7. The ratio of the frequencies at which the secondary peak occurs is $\sim$ 3200 Hz/1750 Hz$\sim$ 1.8.

Run 3 is the same as run 1 except that we use polytropic index $n = 0.5$ ($\Gamma = 3$). This model was run with $N = 1024$ particles per star, with initial separation $a_0 = 4.5R$. The stars first make contact at $t \sim 167t_D$. By the end of the run, the core $\varpi \lesssim 2R$ has 93% of the mass and 67% of the angular momentum; the disk extends out to $\sim 50R$. The gravitational wave forms rh_+ and $rh_\times$ are shown in Fig. 18 for an observer on the axis at $\theta = 0, \phi = 0$. Figure 19(a) shows the gravitational wave luminosity L and 19(b) the energy ΔE emitted as gravitational radiation. Again, the solid lines give the

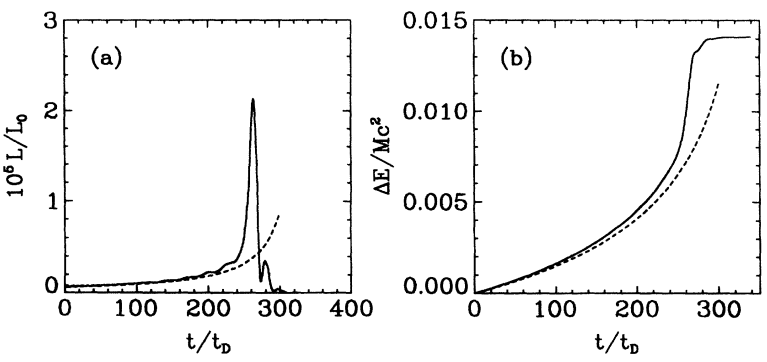

FIG. 16. Various gravitational radiation quantities are shown for run 2. The solid lines show the code results, and the dashed lines the point-mass values; compare with Fig. 7. (a) Gravitational wave luminosity L/L_0; (b) Energy $\Delta E/Mc^2$ emitted as gravitational radiation.

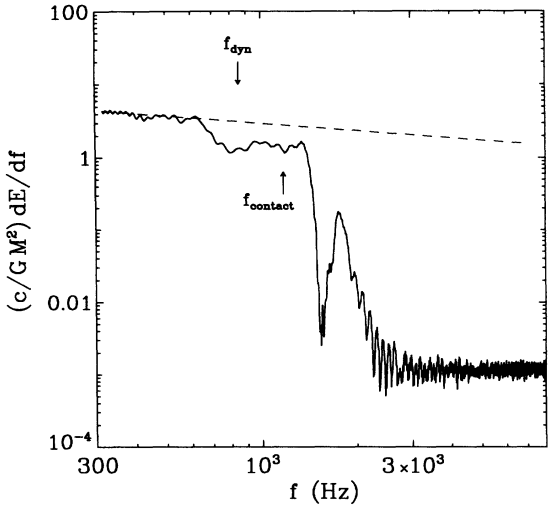

FIG. 17. The gravitational wave-energy spectrum dE/df is shown for run 2; compare with Fig. 12.

code wave forms and the dashed lines the point-mass results. Table II summarizes some features of this run.

However, unlike the previous cases, the core of the merged object is slightly nonaxisymmetric, as shown in Fig. 20. The effect of this rotating, barlike core can be seen in the gravitational wave forms rh_+ and $rh_\times$ in Fig. 18. At late times the angular velocity of the core is $\Omega \sim 0.5t_D^{-1}$, corresponding to a gravitational wave frequency $f \sim 2200$ Hz. This agrees with the wave frequency calculated from Fig. 18 at $t \sim 290t_D$, confirming that the radiation at late times is due to the rotating core. Rasio and Shapiro [14] also found that the coalescence of a synchronized binary with $n = 0.5$ resulted in a rotating barlike core.

The energy spectrum dE/df for run 3 is shown in Fig. 21. Here, the match to point-mass inspiral wave forms occurs at frequency $\sim$ 640 Hz. Dynamical instability is expected to occur at separation $a = 2.76R$ [18], which gives $f_{\rm dyn} = 1342$ Hz. Again we see that the spectrum drops below the point-mass inspiral result near $f_{\rm dyn}$. The spectrum then rises to a sharp peak at $f_{\rm peak} \sim 2200$ Hz, drops sharply, then rises again to a secondary peak at $f_{\rm sec} \sim 2600$ Hz. In this model the gravitational radiation due to the rotating bar is in the frequency range of the first sharp peak. See Table III.

TABLE III. Results of analyzing the simulations in the frequency domain are summarized. All frequencies refer to the spectrum dE/df; cf. Fig. 12. Dynamical instability is expected to occur at separation $a_{\rm dyn}$; these values are taken from [18]. The quantity $f_{\rm dyn}$ is the gravitational wave frequency for point-mass inspiral at separation $a_{\rm dyn}$.

Model	$a_{\rm dyn}$	$f_{\rm dyn}$ (Hz)	$f_{\rm peak}$ (Hz)	$f_{\rm sec}$ (Hz)
Run 1	$2.49R$	1566	2500	3200
Run 2	$2.49R$	852	1500	1750
Run 3	$2.76R$	1342	2200	2600

Lai, Rasio, and Shapiro [18] found that the onset of dynamical instability occurs at separation $a = 2.49R$ for the parameters of run 1 and at $a = 2.76R$ for the parameters of run 3. From this we estimate that the ratio of frequencies at which the various spectral features occur should be $f_{\rm run\ 1}/f_{\rm run\ 3} \sim 1.2$. Our simulations approximate this behavior. For example, the ratio of the frequencies at which the sharp drop occurs is $\sim$ 2500 Hz/2200 Hz$\sim$ 1.1. The ratio of the frequencies at which the secondary peak occurs is $\sim$ 3200 Hz/2600 Hz$\sim$ 1.2.

IX. SUMMARY AND DISCUSSION

We have carried out SPH simulations of the merger and coalescence of identical nonrotating neutron stars modeled as polytropes. The stars start out in the point-mass regime and spiral together due to the effects of gravitational radiation reaction. Once the stars come into contact, they rapidly merge and coalesce. Spiral arms form as mass is shed from the ends of the central rotat-

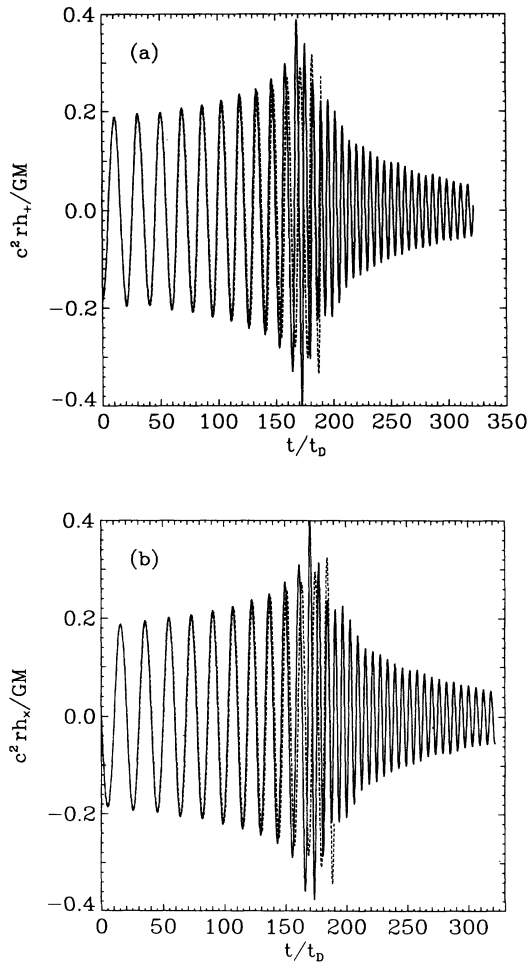

FIG. 18. The gravitational wave forms rh_+ and $rh_\times$ are shown for an observer on the axis at $\theta = 0$, $\phi = 0$ for run 3; compare with Figs. 6 and 15. The solid lines give the code wave forms, and the dashed lines the point-mass results.

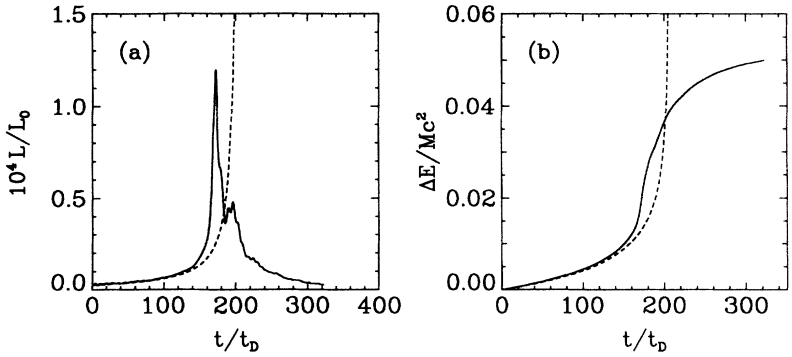

FIG. 19. Various gravitational radiation quantities are shown for run 3; compare with Figs. 7 and 16. The solid lines show the code results, and the dashed lines the point-mass values. (a) Gravitational wave luminosity L/L_0; (b) energy $\Delta E/Mc^2$ emitted as gravitational radiation.

ing barlike structure. Angular momentum is transported outward by gravitational torques and lost to the spiral arms. The arms expand supersonically and merge, forming a shock-heated axisymmetric disk. The central rotating core becomes axisymmetric for $n = 1$, with the gravitational radiation shutting off rapidly after coalescence. For the stiffer equation of state $n = 0.5$, the rotating core is slightly nonaxisymmetric and considerably longer lived, and the gravitational waves decrease more slowly in amplitude.

It is instructive to compare our results with other, related work. Davies *et al.* recently carried out SPH calculations very similar to ours with $n \sim 0.71$ ($\Gamma = 2.4$). Their results for nonrotating stars are similar to ours. Rasio and Shapiro [13,14] have performed SPH simulations of synchronously rotating systems. They found that polytropes with $n = 1$ produce an axisymmetric core, and those with $n = 0.5$ yield a nonaxisymmetric core, in agreement with our results. However, for their synchronously rotating models, the amplitude of the gravitational radiation drops off more rapidly after the merger than in our models. This effect was also seen by Shibata, Nakamura, and Oohara [11] and may be due to the fact that the synchronously rotating stars are not spinning relative to one another when they merge, leading to less "ringing" of the resulting remnant.

We have also calculated the energy emitted in gravitational waves per unit frequency interval dE/df. We find that the spectrum gradually drops below the point-mass inspiral value near the frequency at which the dynamical instability sets in; this causes the stars to spiral together

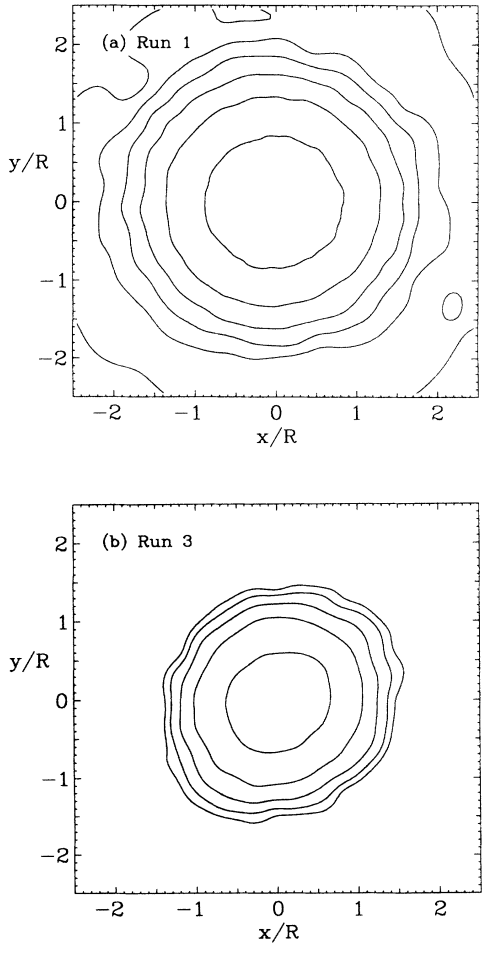

FIG. 20. Density contours are shown for a cut through the $x - y$ plane of the central regions of (a) run 1 ($n = 1$) and (b) run 3 ($n = 0.5$). The same contour levels are plotted in both cases (as in Fig. 2); however, the central density in (b) is lower than the top contour in (a).

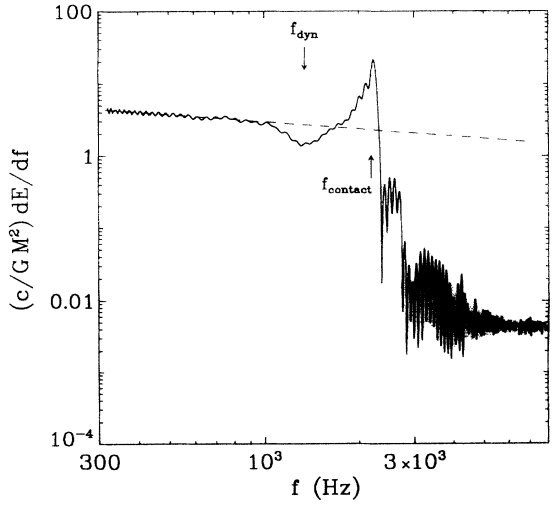

FIG. 21. The gravitational wave-energy spectrum dE/df is shown for run 3; compare with Figs. 12 and 17.

faster than they would on point-mass trajectories. The spectrum then drops sharply near the frequency at which the waves from the main coalescence burst fall off. Finally, the spectrum rises again to a secondary peak at larger frequencies, the result of oscillations that occur during the merger.

The frequencies at which these features in the spectrum occur, as well as their amplitudes, depend on both the neutron-star radius R and the equation of state specified by the polytropic index n. Our standard model, run 1, has $R = 10$ km and $n = 1$. When we change just the radius in run 2 to $R = 15$ km, the spectral features occur at frequencies that are lower by a factor ~ 1.8 and the "gentler" merger leads to a much lower amplitude in the energy spectrum, both near $f_{\rm peak}$ and in the secondary maximum. When instead we change just the polytropic index in run 3 to $n = 0.5$, the features occur at frequencies that are a factor ~ 1.2 lower. The stiffer equation of state results in a longer-lived bar and a substantially stronger peak amplitude. Measurement of the three frequencies $f_{\rm dyn}$, $f_{\rm peak}$, and $f_{\rm sec}$, along with the amplitudes of the spectrum there (relative to the point-mass result), thus may be used to obtain direct information about the physical state of the merging neutron stars. While the details of the peaks depend somewhat on the resolution of our simulations, the general results described here do not.

The gravitational wave forms and the spectrum dE/df contain much information about the hydrodynamical merger and coalescence of binary neutron stars. Our results show that the characteristic frequencies depend on both the neutron-star radii and the polytropic equation of state. We intend to expand our study to include the effects of both spin and nonequal masses, as well as gravitational radiation reaction. In particular, radiation reaction can be expected to affect the evolution of the rotating bar in run 3, leading to changes in the spectrum dE/df. We will present the results of these studies in future papers.

ACKNOWLEDGMENTS

We thank K. Thorne for pointing out the importance of the energy spectrum dE/df and encouraging this work. We also thank M. Davies, D. Kennefick, D. Laurence, and K. Thorne for interesting and helpful conversations, and L. Hernquist for supplying a copy of TREESPH. This work was supported in part by NSF Grants No. PHY-9208914 and No. AST-9308005, and by NASA Grant No. NAGW-2559. The numerical simulations were run at the Pittsburgh Supercomputing Center.

[1] A. Abramovici *et al.*, Science **256**, 325 (1992).
[2] K. Thorne, in *Recent Advances in General Relativity*, edited by A. Janis and J. Porter (Birkhäuser, Boston, 1992).
[3] R. Narayan, T. Piran, and A. Shemi, Astrophys. J. **379**, L17 (1991); E. S. Phinney, *ibid.* **380**, L17 (1991); L. S. Finn and D. Chernoff, Phys. Rev. D **47**, 2198 (1993).
[4] This subject has been developed by many authors; for a recent review see C. Will, in *Proceedings of the Eighth Nishinomiya-Yukawa Symposium on Relativistic Cosmology*, edited by M. Sasaki (Universal Academy Press, Tokyo, in press).
[5] C. Cutler *et al.*, Phys. Rev. Lett. **70**, 2984 (1993).
[6] C. Cutler and E. Flanagan, Phys. Rev. D **49**, 2658 (1994).
[7] B. Meers, Phys. Rev. D **38**, 2317 (1988); K. Strain and B. Meers, Phys. Rev. Lett. **66**, 1391 (1991); A. Krolak, J. Lobo, and B. Meers, Phys. Rev. D **43**, 2470 (1991); **47**, 2184 (1993).
[8] W. Johnson and S. Merkowitz, Phys. Rev. Lett. **70**, 2367 (1993); W. Hamilton (private communication); H. Paik (private communication).
[9] D. Kennefick, D. Laurence, and K. Thorne (unpublished).
[10] L. Lindblom, Astrophys. J. **398**, 569 (1992).
[11] M. Shibata, T. Nakamura, and K. Oohara, Prog. Theor. Phys. **88**, 1079 (1992).
[12] See also K. Oohara and T. Nakamura, Prog. Theor. Phys. **82**, 535 (1989); **83**, 906 (1990); T. Nakamura and K. Oohara, *ibid.* **82**, 1066 (1989); **86**, 73 (1991).
[13] F. Rasio and S. Shapiro, Astrophys. J. **401**, 226 (1992).
[14] F. Rasio and S. Shapiro, Astrophys. J. **432**, 242 (1994).
[15] M. Davies, W. Benz, T. Piran, and F. Thielemann, Astrophys. J. **431**, 742 (1994).
[16] J. Zahn, Astron. Astrophys. **57**, 383 (1977).
[17] C. Kochanek, Astrophys. J. **398**, 234 (1992); L. Bildsten and C. Cutler, *ibid.* **400**, 175 (1992).
[18] D. Lai, F. Rasio, and S. Shapiro, Astrophys. J. **420**, 811 (1994).
[19] D. Lai, F. Rasio, and S. Shapiro, Astrophys. J. **403**, L63 (1993); Astrophys. J. Suppl. **88**, 205 (1993).
[20] L. Kidder, C. Will, and A. Wiseman, Phys. Rev. D **47**, 3281 (1993).
[21] L. Lucy, Astron. J. **82**, 1013 (1977); R. Gingold and J. Monaghan, Mon. Not. R. Astron. Soc. **181**, 375 (1977); see J. Monaghan, Annu. Rev. Astron. Astrophys. **30**, 543 (1992) for a review.
[22] L. Hernquist and N. Katz, Astrophys. J. Suppl. **70**, 419 (1989).
[23] J. Barnes and P. Hut, Nature (London) **324**, 446 (1986); L. Hernquist, Astrophys. J. Suppl. **64**, 715 (1987).
[24] J. Centrella and S. McMillan, Astrophys. J. **416**, 719 (1993).
[25] J. Houser, J. Centrella, and S. Smith, Phys. Rev. Lett. **72**, 1314 (1994); J. Houser, S. Smith, and J. Centrella (unpublished).
[26] C. Misner, K. Thorne, and J. Wheeler, *Gravitation* (Freeman, New York, 1973).
[27] C. Kochanek, S. Shapiro, S. Teukolsky, and D. Chernoff, Astrophys. J. **358**, 81 (1990).
[28] K. Thorne, in *300 Years of Gravitation*, edited by S. Hawking and W. Israel (Cambridge University Press, New York, 1987).
[29] L. S. Finn and C. Evans, Astrophys. J. **351**, 588 (1990).
[30] S. Shapiro and S. Teukolsky, *Black Holes, White Dwarfs, and Neutron Stars* (Wiley, New York, 1983).
[31] D. Gilden and S. Shapiro, Astrophys. J. **287**, 728 (1984).
[32] K. Thorne (private communication).
[33] J. Cox, *Theory of Stellar Pulsation* (Princeton University Press, Princeton, 1980).

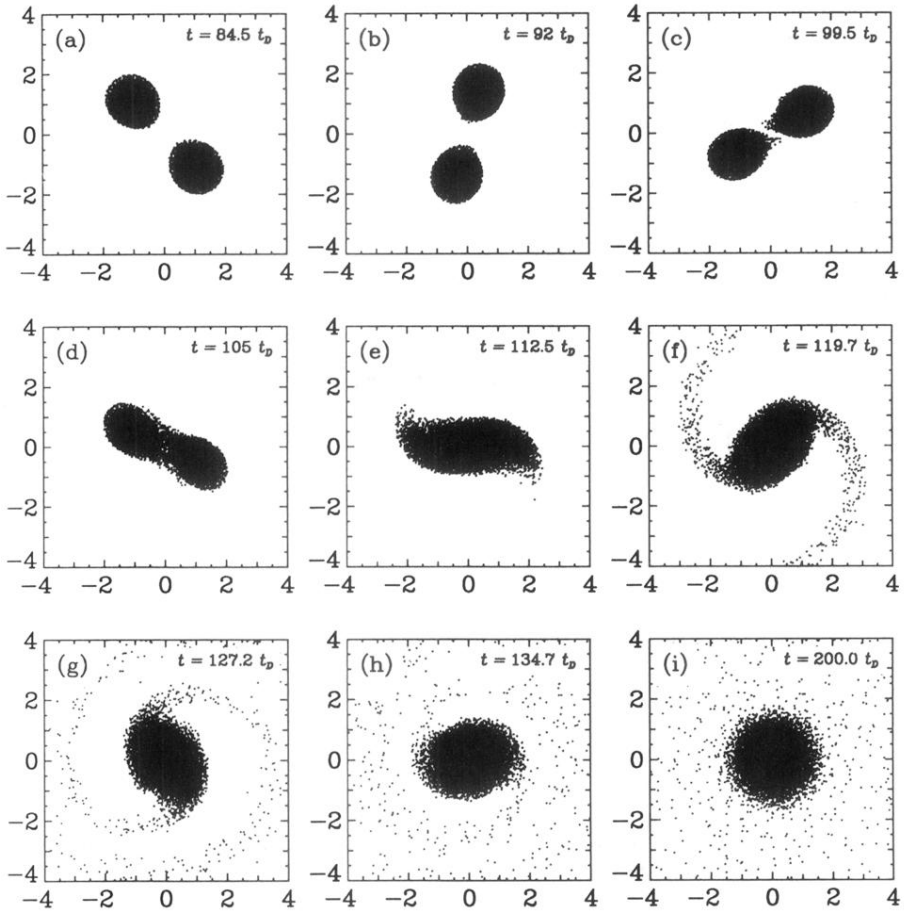

FIG. 1. Particle positions are shown projected onto the x-y plane for run 1 with $N = 4096$ particles per star. Here, $M = 1.4\ M_\odot$, $R = 10$ km, polytropic index $n = 1$, and initial separation $a_0 = 4R$. The stars are orbiting in the counterclockwise direction. The vertical axis in each frame is y/R and the horizontal axis is x/R.

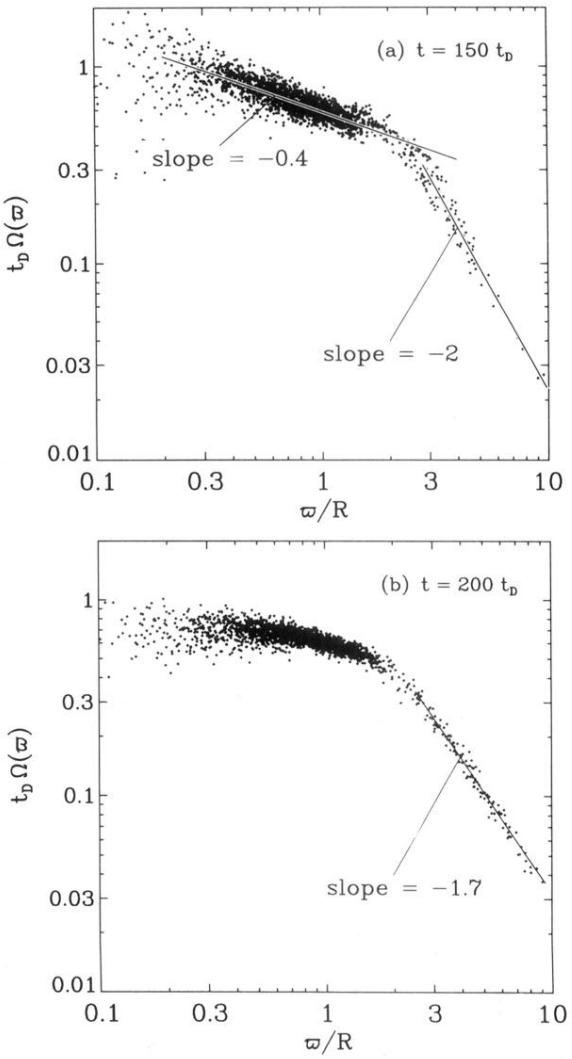

FIG. 3. The angular velocity $\Omega(\varpi)$, where $\varpi = (x^2 + y^2)^{1/2}$, is shown for run 1 with $N = 4096$ particles per star. $\Omega = 1$ (i.e., t_D^{-1}) corresponds to a spin period $T_{\rm spin} = 0.46$ ms. (a) $t = 150 t_D$, (b) $t = 200 t_D$.